

Conductivity of ZnO Nanowires, Nanoparticles, and Thin Films Using Time-Resolved Terahertz Spectroscopy[†]

Jason B. Baxter and Charles A. Schmuttenmaer*

Chemistry Department, Yale University, P.O. Box 208107, 225 Prospect Street,
New Haven, Connecticut 06520-8107

Received: July 12, 2006; In Final Form: August 17, 2006

The terahertz absorption coefficient, index of refraction, and conductivity of nanostructured ZnO have been determined using time-resolved terahertz spectroscopy, a noncontact optical probe. ZnO properties were measured directly for thin films and were extracted from measurements of nanowire arrays and mesoporous nanoparticle films by applying Bruggeman effective medium theory to the composite samples. Annealing significantly reduces the intrinsic carrier concentration in the ZnO films and nanowires, which were grown by chemical bath deposition. The complex-valued, frequency-dependent photoconductivities for all morphologies were found to be similar at short pump–probe delay times. Fits using the Drude–Smith model show that films have the highest mobility, followed by nanowires and then nanoparticles, and that annealing the ZnO increases its mobility. Time constants for decay of photoinjected electron density in films are twice as long as those in nanowires and more than 5 times those for nanoparticles due to increased electron interaction with interfaces and grain boundaries in the smaller-grained materials. Implications for electron transport in dye-sensitized solar cells are discussed.

Introduction

Performance of devices based on semiconductor nanomaterials can depend sensitively on the nanostructure morphology. For instance, dye-sensitized solar cells (DSSCs) employ a high surface area, mesoporous semiconductor to transport electrons injected from photoexcited dye molecules to the conducting substrate.^{1,2} The conductivity of this mesoporous, nanocrystalline material differs significantly from that of bulk single-crystal samples.^{3,4} The nanocrystalline semiconductor film is typically $\sim 10\ \mu\text{m}$ thick and consists of $\sim 10\ \text{nm}$ diameter TiO_2 or ZnO nanoparticles, and injected electrons hop from particle to particle to reach the substrate.^{5,6} ZnO has shown efficiencies of 5% in nanoparticle-based DSSCs, second only to TiO_2 (10%).² ZnO and TiO_2 have similar band positions, and the cause of the difference in efficiencies between the two materials is a topic of current research.^{7,8} Unlike TiO_2 , ZnO has the advantage that its crystal structure allows it to be grown anisotropically such that DSSCs based on nanowire arrays are possible. Recent work has suggested that dense arrays of ZnO nanowires could improve electron transport by providing direct conduction pathways to the substrate while maintaining high surface area.^{9–11} Hybrid DSSCs, which employ nanowire arrays with nanoparticles filling the interstitial spaces, have shown promise as a means of combining the high surface area of nanoparticles with direct transport through nanowires.¹² Intensity-modulated photocurrent spectroscopy (IMPS) and transient photocurrent time-of-flight (TOF) are optical pump/electrical probe techniques, and they have been the primary methods used to study macroscopic electron transport through the mesoporous semiconductor.^{13–15} However, IMPS and TOF cannot provide information on very short time and length scales.

Time-resolved terahertz spectroscopy (TRTS) is an excellent complement to IMPS and TOF measurements because it measures the complex-valued, frequency-dependent, far-infrared photoconductivity on sub-picosecond to nanosecond time scales using an optical pump and a terahertz probe. TRTS is an ideal technique for studying conductivity because it probes the far-infrared ($0.2\text{--}2\ \text{THz}$ or $6\text{--}66\ \text{cm}^{-1}$) region of the spectrum, which closely matches typical carrier scattering rates of 10^{12} to $10^{14}\ \text{s}^{-1}$.^{3,16} Terahertz time-domain spectroscopy (THz-TDS), a static variation of TRTS without the optical pump, has been used to measure the native conductivity and carrier density of doped Si and GaAs wafers.^{17,18} THz-TDS and TRTS can provide more detailed information on conductivity than other optical techniques such as Fourier transform infrared (FTIR) spectroscopy for two reasons. First, TRTS and THz-TDS measure both the amplitude and the phase of single-cycle oscillations of the terahertz electric field and do not require a Kramers–Kronig analysis to extract the absorption coefficient and refractive index. Second, the terahertz frequency range is on the order of the carrier scattering time, allowing more accurate modeling of the data. Furthermore since TRTS is a noncontact optical probe of electrical properties, it eliminates the need for and complications from forming ohmic contacts and attaching lead wires to the semiconductor, making it ideal for probing semiconductor nanomaterials. TRTS has recently been used to study photoconductivity in nanomaterials such as microcrystalline Si thin films,¹⁹ TiO_2 nanoparticle films,^{3,4} CdSe quantum dots,²⁰ and InP quantum dots and arrays.²¹

When porous nanomaterials are investigated using terahertz spectroscopy, it is appropriate to use effective medium theory because the wavelength of the probe radiation ($150\ \mu\text{m}\text{--}1.5\ \text{mm}$) is much larger than the characteristic particle dimensions.²² Effective medium theory is most often used to calculate the permittivity of a composite material given the permittivity and volume fraction of each of the individual components. However,

[†] Part of the special issue “Arthur J. Nozik Festschrift”.

* Author to whom correspondence should be addressed. E-mail: charles.schmuttenmaer@yale.edu.

it can also be used in reverse to calculate the permittivity of one component when the other component and the composite permittivities are known. This “reverse effective medium theory” approach has been used by Black et al. to calculate the absorption coefficient and refractive index of an array of bismuth nanowires using FTIR spectroscopy,²³ and it is the method employed in this work.

The Bruggeman effective medium approximation (EMA)²⁴ and Maxwell–Garnett theory (MGT)²⁵ are two of the most commonly used effective medium theories. They are both based on the Lorentz–Lorenz Clausius–Mossotti equation but with slightly different assumptions, and each has advantages and limitations.²² For example, MGT has been used to fit the composite permittivity of a mesoporous TiO₂ nanoparticle film using the permittivities of bulk TiO₂ and air.⁴ However, we found that using reverse MGT to calculate nanostructure permittivities from composite measurements does not give robust and reliable results in our case because of singularities in the model that occur for the large nanostructure volume fractions and large contrast ratios of the individual component permittivities. Therefore, we use the Bruggeman EMA and find that it works very well. The Bruggeman EMA is given by

$$f \left(\frac{\epsilon_p - \epsilon}{\epsilon_p + K\epsilon} \right) + (1 - f) \left(\frac{\epsilon_m - \epsilon}{\epsilon_m + K\epsilon} \right) = 0 \quad (1)$$

where f is the particle volume fraction, ϵ is the composite permittivity, ϵ_m is the matrix permittivity, ϵ_p is the particle permittivity, and K is a geometric factor. K is 1 for an array of cylinders with its axis collinear with the incident radiation and 2 for spherical nanoparticles.²³

THz-TDS and TRTS have recently been used in the first terahertz studies of ZnO.^{26,27} ZnO is a wide band gap semiconductor ($E_g = 3.37$ eV) with optoelectronic properties that have allowed its use in applications such as transparent conducting oxides films,²⁸ field effect transistors,²⁹ sensors,³⁰ optically pumped UV lasers,³¹ and DSSCs.^{2,9–12} Initial terahertz work on ZnO measured the terahertz absorption coefficient, refractive index, and photoconductivity of high-resistivity, single-crystal ZnO wafers. Azad and co-workers found that the absorption coefficient of a ZnO wafer with low electron density was nearly zero and that its terahertz index of refraction was fairly constant at 2.8.²⁶ A small absorption coefficient increase with increasing frequency was attributed to the tail of a phonon mode at 12.4 THz. Hendry et al. investigated the generation of free electrons and holes and the subsequent formation of excitons in photoexcited ZnO wafers at temperatures below 150 K.²⁷ In this article, we use both THz-TDS and TRTS to determine both native and photoinduced conductivity as a function of morphology and postgrowth annealing treatments for ZnO nanowire arrays, mesoporous nanoparticle films, and continuous thin films.

Experimental Methods

An amplified Ti:sapphire laser (Tsunami/Spitfire from Spectra Physics) is used to generate 800 mW of pulsed near-IR light at 1 kHz. The pulse width is ~ 100 fs, and the center wavelength is 775 nm. For pump–probe studies, about two-thirds of the power is frequency-doubled to produce 120 mW of 387 nm light for the pump beam. The remainder of the near-IR light is used to generate and detect terahertz radiation using a four-parabola arrangement that focuses the terahertz radiation to a spot size of ~ 3 mm at the sample. Terahertz radiation is generated using optical rectification in a ZnTe crystal and detected using free-space electrooptic sampling in a second ZnTe

crystal. More details on the TRTS spectrometer have been published previously.¹⁶ Since the higher terahertz frequencies are more tightly focused at the sample, care was taken to ensure that the pump beam spot size was significantly larger than the terahertz spot size for frequency-dependent studies.

All of the ZnO morphologies were grown or deposited to thicknesses of ~ 4 μm on 2 cm \times 2 cm, 160- μm -thick glass cover slips. ZnO nanoparticles (Aldrich) were suspended in a 25 wt % solution in ethanol and doctor-bladed onto the cover slip using a Scotch tape mask.² The nanoparticle film was then annealed in air at 360 °C for 30 min to promote sintering and substrate adhesion. ZnO nanowires and films were grown by chemical bath deposition.^{10,32} A ~ 10 nm ZnO seed film was first deposited on the substrate by drop-coating with a 5 mM solution of zinc acetate in ethanol, rinsing, and drying.³³ This sequence was repeated five times, then the substrate was annealed in air at 320 °C for 20 min, and the entire process was repeated again. Seeded substrates were placed in an aqueous solution of zinc nitrate and methenamine and heated in a closed vial at 85 °C for 3 h. Samples were then removed from solution, rinsed with water, and placed in a fresh batch of precursor solution, and the growth process was repeated. For nanowires, the growth process was repeated eight times with 25 mM zinc nitrate and methenamine concentrations. For films, the growth process was repeated two times with precursor concentrations of 0.10 M. Some film and nanowire samples were characterized without further processing, which we will refer to as “as-grown”, while others were annealed in air at 360 °C for 30 min. ZnO was then removed from half of the sample by dipping in 25% v/v acetic acid in deionized water for 2 min, allowing subsequent determination of the substrate optical properties.

The absorption coefficient and index of refraction of the ZnO/air composite are determined from a series of time-domain terahertz scans, and the ZnO properties are then calculated from the composite properties using effective medium theory. Time-domain scans are taken of air, the cover slip, and the ZnO/air composite on the cover slip. The air, cover slip, and composite time-domain scans are each Fourier transformed, and the absorption coefficient and refractive index are calculated from the power and phase as a function of frequency. We use the method of complex impedance for waves in layered media, described by Brekhovskikh,³⁴ to account for reflections that occur in the thin glass substrates and ZnO samples. We calculate the absorption coefficient and refractive index of the cover slip using the air and cover slip scans, then we use these values along with the Fourier transformed composite scan to determine the absorption coefficient and refractive index of the ZnO/air composite. ZnO absorption coefficient and refractive index are calculated by employing the reverse EMA with the composite data.

For photoconductivity studies, the difference between the photoexcited and the non-photoexcited sample is also recorded in the time-domain and added to the composite scan to create a photoexcited composite waveform. Because the difference in signal intensity between photoexcited and non-photoexcited samples is 2 orders of magnitude smaller than the signal itself, this difference method allows much more accurate determination of the photoconductivity. Figure 1 shows an 8 ps portion of the 20 ps time-domain scans for the reference, cover slip, ZnO/air composite on cover slip, and photoexcitation difference scan as well as the sum of the ZnO/air and difference scans, i.e., the photoexcited waveform.

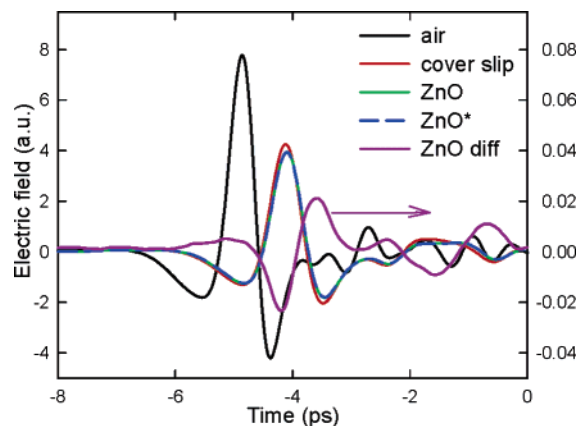


Figure 1. Time-domain terahertz waveforms with air, cover slip, and ZnO composite at the terahertz focus. The photoexcited ZnO difference waveform (right axis) is added to the ZnO composite waveform to generate the photoexcited ZnO* composite waveform.

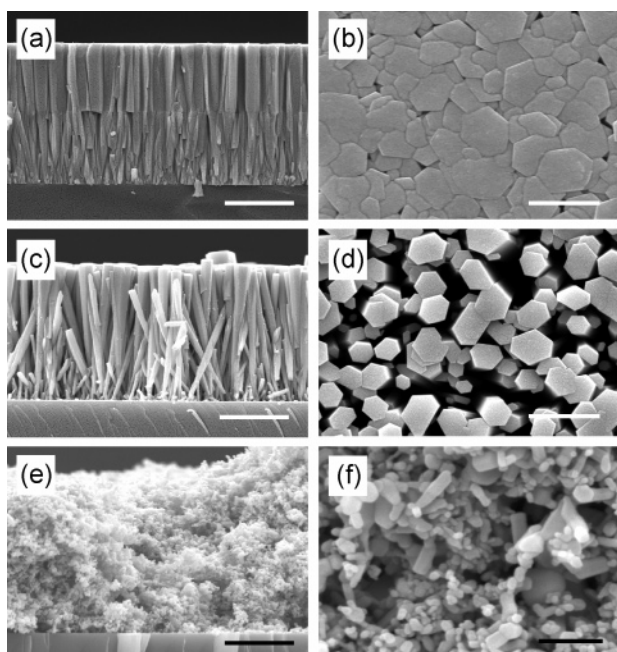


Figure 2. Cross-sectional (left column) and plan view (right column) scanning electron micrographs of (a and b) ZnO continuous thin film, (c and d) nanowire array, and (e and f) mesoporous nanoparticle film. Scale bars are 2 μm in parts a, c, and e, 1 μm in parts b and d, and 500 nm in part f.

Results and Discussion

Static ZnO Properties. ZnO thin films, nanowires, and nanoparticle films were grown or deposited on thin glass cover slips to study the effect of morphology on the terahertz absorption coefficient, index of refraction, and conductivity. Cross-sectional and plan view scanning electron micrographs of each of the morphologies are shown in Figure 2. Both ZnO films and nanowires have the hexagonally symmetric wurtzite crystal structure and are oriented with the *c*-axis perpendicular to the substrate. The thin films, Figures 2a and 2b, are continuous and polycrystalline with a thickness of 4.5 μm . The films consist of hexagonal, columnar grains with average diameters of ~ 500 nm that grow perpendicular to the substrate. The void fraction is very small, and for the purpose of the EMA we assume a volume fraction of 1. The nanowires, Figures 2c and 2d, grow approximately perpendicular to the substrate in dense arrays with lengths of 4 μm . The nanowires are single crystals and are slightly tapered, with diameters of ~ 100 nm

near the base and ~ 200 nm near the top. The volume fraction of nanowires is estimated to be 60% by examining plan view scanning electron microscopy images. The ZnO nanoparticles, Figures 2e and 2f, form a mesoporous film of randomly oriented nanocrystals. The nanocrystals are primarily spherical with some elliptical particles and have sizes in the 20–100 nm range. The nanoparticle film is 4 microns thick, and the volume fraction is estimated to be 50%.

The ZnO absorption coefficient and refractive index are calculated from the ZnO/air composite absorption coefficient and refractive index using the reverse Bruggeman EMA. Rearranging eq 1 to solve for the particle permittivity, ϵ_p , with ϵ_m equal to unity for air, gives

$$\epsilon_p = \frac{\epsilon[f(1 + K\epsilon) + (1 - f)K(\epsilon - 1)]}{f(1 + K\epsilon) + (1 - f)(1 - \epsilon)} \quad (2)$$

The complex permittivity and complex refractive index are related by $\hat{\epsilon} = \hat{n}^2$.

Figures 3a and 3c show the *composite* absorption coefficient and refractive index for each of the five samples from 0.2 to 1.6 THz, while Figures 3b and 3d show the absorption coefficient and refractive index of ZnO in the composite calculated using the reverse EMA. The composite data show that annealed films, nanowires, and nanoparticles each have absorption coefficient of nearly zero, while as-grown nanowires and films have an absorption coefficient that increases with increasing frequency. The composite nanoparticle absorbance is sometimes negative as a result of the noise inherent in measuring the negligible absorbance of a very thin film. The as-grown film has a refractive index of ~ 4 –5, the annealed film and as-grown nanowires have a refractive index of 3, and the nanoparticle and annealed nanowire composites have refractive index of 2. The as-grown film and nanowires have refractive indices that decrease with increasing frequency.

Figures 3b and 3d display the absorption coefficient and refractive index of the ZnO itself, as calculated using eq 2 with $K = 1$ for nanowires and $K = 2$ for nanoparticles. The absorption coefficient and refractive index of ZnO are greater than those of the composite, as expected since the composite is a mixture of ZnO and air permittivities. ZnO and composite permittivities are equal for the films, since films have a volume fraction of 1. The annealed ZnO thin films, nanowires, and nanoparticle films all have nearly zero Napierian power absorption coefficient (less than 150 cm^{-1}) and a refractive index of approximately 3.0 over this frequency range. By comparison, the absorption coefficient and refractive index of a high-resistivity, single-crystal ZnO wafer are less than 10 cm^{-1} and 2.8, respectively.²⁶ The absorption coefficient and refractive index of the annealed ZnO are very similar to each other and to bulk ZnO, indicating that our use of the EMA is appropriate and our estimations of volume fractions are accurate. The small differences between samples likely result from small errors in the determination of composite thickness and volume fraction, from assumptions made by the EMA, and from differences in the ZnO purity and conductivity.

The absorption coefficient and refractive index of the thin film and nanowire array that have not been annealed are much larger than those of the annealed samples, as shown in Figure 3. ZnO film and nanowire absorption coefficients are very similar to each other, increasing steadily from 200 cm^{-1} at 0.2 THz to over 800 cm^{-1} at 1.6 THz. The film refractive index is about 6 at low frequency and decreases to below 4 at 1.6 THz, while the nanowire refractive index decreases from 7 to 5. The larger absorption coefficient and refractive index for the as-

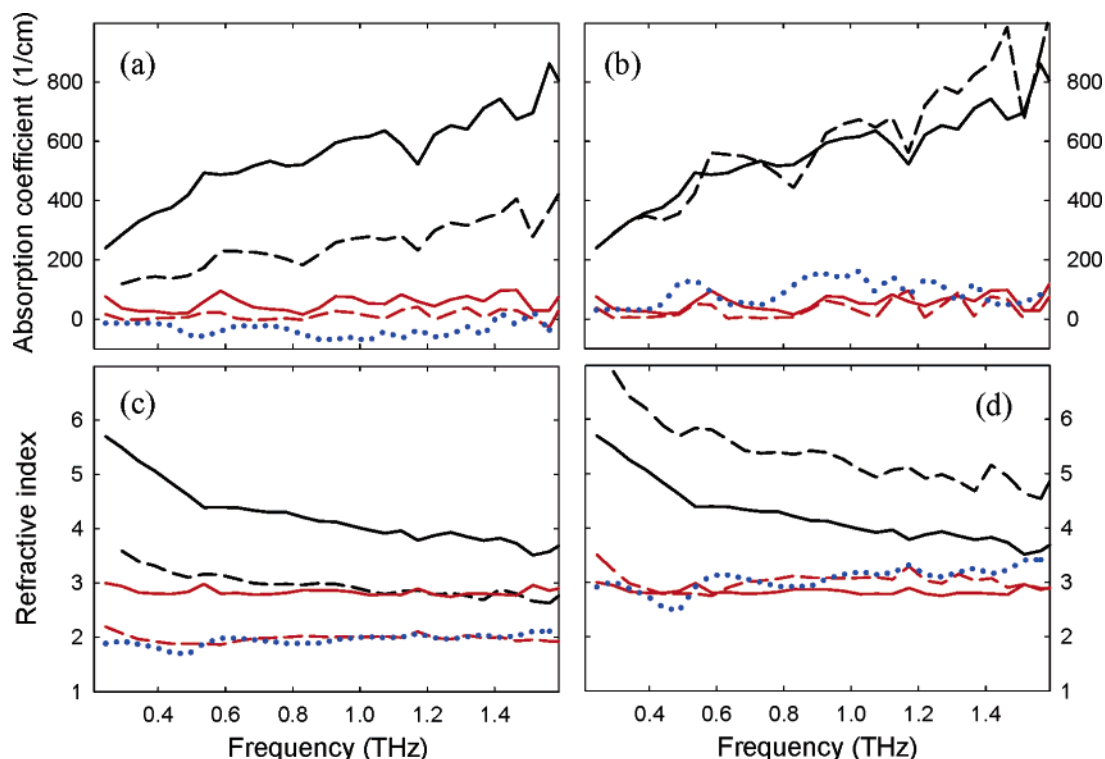


Figure 3. (a and b) Absorption coefficients and (c and d) refractive indices of ZnO/air composite (left column) and of ZnO itself (right column). ZnO values are extracted from the composite data using the reverse EMA. Solid lines are for ZnO films, dashed lines for nanowires, and blue dotted lines for nanoparticles. Black lines refer to as-grown samples, and red lines refer to annealed samples. This scheme is used where applicable in subsequent figures.

grown samples compared to those of annealed samples are due to mobile electrons in the conduction band. As-grown ZnO is frequently n-type due to oxygen or zinc vacancies or interstitials,³⁵ but annealing can make the lattice more stoichiometric by reducing the concentration of these defects.^{32,36}

The native conductivity, $\hat{\sigma}$, of the as-grown samples was determined using the absorption coefficient and refractive index of the annealed sample for the static permittivity, $\hat{\epsilon}$, and those of the as-grown samples for the generalized permittivity, $\hat{\eta}$, in

$$\hat{\eta}(\omega) = \hat{\epsilon}(\omega) + \frac{i\hat{\sigma}(\omega)}{\epsilon_0\omega}, \quad (3)$$

where ω is the angular frequency, ϵ_0 is the free-space permittivity, and i is the unit imaginary. $\hat{\eta}$, $\hat{\epsilon}$, and $\hat{\sigma}$ are complex and frequency-dependent. Note that the absorption coefficient and refractive index of the ZnO itself, not the composite, are used to calculate the ZnO conductivity. We attribute all measured conductivity to electrons and not holes because intrinsic ZnO is always n-type, with donor densities often an order of magnitude larger than acceptor densities.³⁷ Additionally, the effective mass of the electron in ZnO is about half that of the hole, so electron mobility will be larger and free carrier terahertz absorption will be greater than that for holes.³⁸ The frequency-dependent complex conductivity is shown in Figure 4a for as-grown nanowires and films. The real part of the conductivity is positive and increasing with increasing frequency, while the imaginary component is negative and decreasing with increasing frequency. Figure 4b shows the native conductivity of the annealed film using an absorption coefficient of 0 and a refractive index of 2.8 for the static permittivity, as determined by Azad for a high-resistivity ZnO wafer.²⁶ We have independently confirmed these benchmark values for the bulk, single-crystal absorption coefficient and refractive index using a ZnO

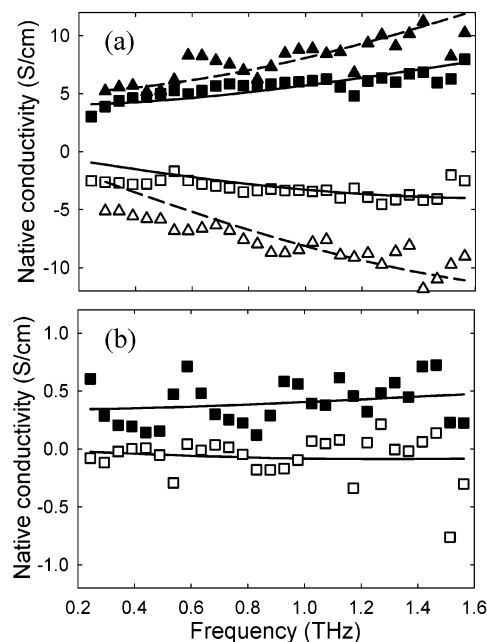


Figure 4. Measured native conductivity (points) of ZnO films and nanowires with fits of the Drude–Smith model (lines). Part a shows as-grown films (squares, solid lines) and as-grown nanowires (triangles, dashed lines). Part b shows annealed films. Solid symbols are the real component of the conductivity, and open symbols are the imaginary component.

wafer with higher defect density that was cooled to 10 K. Again, the real part is positive and increasing with increasing frequency, and the imaginary part is negative, but the conductivity of the annealed samples is about an order of magnitude smaller than that for the as-grown samples. The conductivity is a function of electron density and scattering time, and we can extract these

parameters from the data by fitting the conductivity with an appropriate model.

The Drude model is the most common and straightforward model for conductivity in metals and semiconductors, but it does not fit the data presented here. The Drude model considers a free electron gas with complete momentum randomization following elastic scattering events, and it dictates that the real component of the conductivity has its maximum value at direct current (DC) and that the imaginary component is positive with a maximum at the frequency of the carrier scattering rate. The Drude model cannot produce either real conductivity with a non-DC maximum or negative imaginary conductivity.

Negative imaginary conductivity in ZnO and TiO₂ has been attributed to phenomena such as backscattering of electrons at interfaces and surfaces,³ consequences of the effective medium theory,⁴ and the polarizability of excitons.²⁷ Since the ZnO is not being photoexcited, excitons should not be present and cannot contribute to the native conductivity. The negative conductivity also cannot be attributed to the effective medium theory because it occurs for the continuous thin films that have a volume fraction of 1 and so are not subject to effective medium theory. Additionally, we have used the Bruggeman EMA to determine the ZnO permittivity from the composite permittivity and have seen that the negative imaginary conductivity of the composite is a consequence of the negative imaginary conductivity of the ZnO particles.

We attribute the negative imaginary conductivity to preferential backward scattering of electrons after collisions. A fraction, but not all, of the backward scattering is a result of the electron reflecting from surfaces or grain boundaries or defects. It could also result from a Coulombic restoring force from positively charged holes or defects. This restoring force or backward scattering can be modeled by modifying the Drude model according to Smith by including a persistence of velocity parameter to describe the scattering event.³⁹ The Drude–Smith model is given by

$$\hat{\sigma}(\omega) = \frac{\epsilon_0 \omega_p^2 \tau}{(1 - i\omega\tau)} \left[1 + \sum_{n=1}^{\infty} \frac{c_n}{(1 - i\omega\tau)} \right] \quad (4)$$

Furthermore, the electron density and plasma frequency are related through

$$N_e = \frac{\epsilon_0 \omega_p^2 m^*}{e^2} \quad (5)$$

The summation in eq 4 is often truncated after the first term, where c_1 is the expectation value of the cosine of the scattering angle, ω_p is the plasma frequency, N_e is the electron density, m^* is the electron effective mass which is 0.24 m_e for ZnO,³⁸ and τ is the characteristic scattering time. A value of c_1 less than -0.5 results in negative imaginary conductivity at low frequencies, and c_1 equal to zero recovers the Drude model. The Drude–Smith model has reproduced the conductivity behavior of a variety of poor metals such as expanded liquid Hg, liquid Te, and Al_{63.5}Cu_{24.5}Fe₁₂ quasicrystals³⁹ as well as that of semiconductors such as TiO₂ nanoparticle arrays.³

The Drude–Smith model fits the conductivity quite well for each of the three samples, as shown in Figure 4. We use N_e , τ , and c_1 as adjustable parameters, and the fitted parameters for each case are shown in Table 1. The native carrier concentrations in as-grown nanowires, the as-grown ZnO thin films, and the annealed films are 1.9×10^{18} , 6.1×10^{17} , and $2.5 \times 10^{16} \text{ cm}^{-3}$, respectively. The annealed ZnO film has a carrier concentration

TABLE 1: Parameters for Drude–Smith Fits of Native Conductivity^a

	N_e (10^{17} cm^{-3})	τ (fs)	c_1
nanowires	19	28	−0.92
film	6.1	35	−0.84
annealed film	0.25	39	−0.7

^a Electron density, scattering time, and persistence of velocity for the best fit of the Drude–Smith model, eq 4, to measured native conductivities of three ZnO samples. Data and fits are shown in Figure 4.

$2.5 \times 10^{16} \text{ cm}^{-3}$ larger than that of the highly resistive wafer reported by Azad. The 90% confidence intervals for the parameters, assuming standard errors in conductivity of 1 S/cm, are typically about $\pm 50\%$ for N_e , ± 10 fs for τ , and ± 0.03 for c_1 for the as-grown samples. The annealed film can be fit with a larger range of parameters because the frequency-dependent conductivity is rather flat; thus, confidence intervals are about 5 times those of the as-grown samples. The scattering times for each of the three samples are effectively the same, ~ 35 fs, within the variance of the model fit. The persistence of velocity parameter, c_1 , is least negative for the annealed films and closest to -1 for the as-grown nanowires. These data demonstrate that annealing reduces the native carrier concentration in the ZnO samples, presumably by making the lattice more stoichiometric by eliminating ionized oxygen vacancies and interstitials. Annealing also makes c_1 less negative, indicating that the ZnO is becoming more like an ideal Drude conductor. The DC mobility for a Drude conductor is given by

$$\mu = \frac{e\tau}{m^*} \quad (6)$$

However, materials that obey Drude–Smith conductivity behavior have DC mobilities of $(1 + c_1)\mu$, which is about 20% of the Drude mobility for our ZnO films and nanowires. The DC mobilities calculated using τ and c_1 from Table 1 are 16, 40, and 84 $\text{cm}^2 \text{ V}^{-1} \text{ s}^{-1}$ for nanowires, thin films, and annealed thin films, respectively.

Mobilities can vary widely depending on morphology, microstructure, and growth conditions. However, our measured mobilities agree well with literature values of comparable ZnO materials that have been measured using both electrical and optical probes. As expected, the mobilities in our nanowires and polycrystalline films grown at low temperature are lower than those of bulk, single-crystal ZnO wafers, which were found to have Hall mobilities of $200 \text{ cm}^2 \text{ V}^{-1} \text{ s}^{-1}$ at 300 K.³⁷ Current–voltage measurements of individual nanowires tested in a two-point configuration have shown mobilities of $9 \text{ cm}^2 \text{ V}^{-1} \text{ s}^{-1}$, with mobilities varying slightly as a function of nanowire dimensions.⁴⁰ Hall measurements on polycrystalline ZnO thin films typically fall in the $5\text{--}60 \text{ cm}^2 \text{ V}^{-1} \text{ s}^{-1}$ range.⁴¹ Optical measurements, using attenuated total reflection FTIR, on polycrystalline ZnO thin films grown by metal–organic chemical vapor deposition, show mobilities of $10\text{--}12 \text{ cm}^2 \text{ V}^{-1} \text{ s}^{-1}$.⁴² The DC resistivity of the as-grown films is $0.25 \text{ } \Omega \text{ cm}$, in the range of what is expected for undoped ZnO thin films and single crystals.⁴¹

Pump–Probe Studies. In addition to studying the static properties of the ZnO films, nanowires, and nanoparticles, we have also investigated their response to near-UV photoexcitation. Two types of photoexcitation studies were undertaken. In the first study, so-called “pump scans” monitor the difference between photoexcited and non-photoexcited samples at the peak

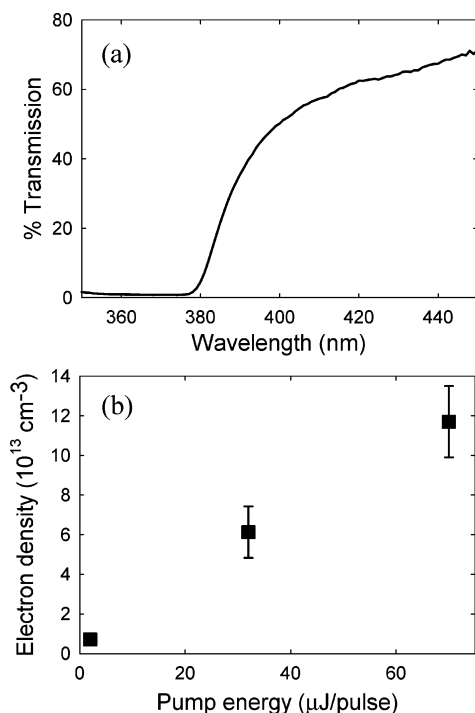


Figure 5. (a) UV-vis transmission spectrum of a continuous ZnO film showing band edge absorbance near 387 nm. (b) Change in electron density upon photoexcitation of a ZnO wafer as a function of pump beam power. Electron density is calculated from the Drude model fit to the photoconductivity, with error bars representing 90% confidence intervals. The linear relationship indicates electron injection results from a single-photon absorption process.

of the terahertz waveform while changing the pump-probe delay time.¹⁶ These pump scans were used to investigate the dynamics of both the onset and decay of photoconductivity. In the second study, “difference scans”, as shown in Figure 1, were taken of the ZnO samples that show the difference in the terahertz waveform between photoexcited and non-photoexcited samples at a fixed pump-probe delay time.¹⁶ These difference scans, combined with the three scans that determine the static properties, are used to calculate the frequency-dependent, complex-valued photoconductivity.

The band gap of ZnO is ~ 3.2 eV, or ~ 387 nm, at room temperature. The amplified Ti:sapphire laser can be tuned over the range 750–830 nm so that the center wavelength of the frequency-doubled pump beam is tunable from 375 to 415 nm. Figure 5a shows the UV-vis transmission spectrum of an as-grown ZnO film. The tunable wavelength range of the pump pulse brackets the band gap of the ZnO. The film is partially scattering to visible light, so the nontransmitted light could be either absorbed or reflected. We chose a pump wavelength that is centered at 387 nm, extending ± 3 nm (full width at half-maximum) due to the 100 fs pulse width. The UV-vis spectrum at 387 nm and transmission measurements using the laser pump pulse both show $\sim 33\%$ transmission through the film, with $\sim 67\%$ absorbed or scattered. Using this wavelength allows high photon absorption while keeping the optical skin depth larger than the film thickness. Although absorption decays exponentially through the film according to Beer’s law, the large optical skin depth allows us to approximate the absorption coefficient as uniform throughout the thickness of the film.¹⁶ The nanowire and nanoparticle samples were too highly scattering to make accurate transmission measurements. However, photoluminescence, X-ray diffraction, and transmission electron microscopy confirm that the nanowires and nanoparticles are crystalline

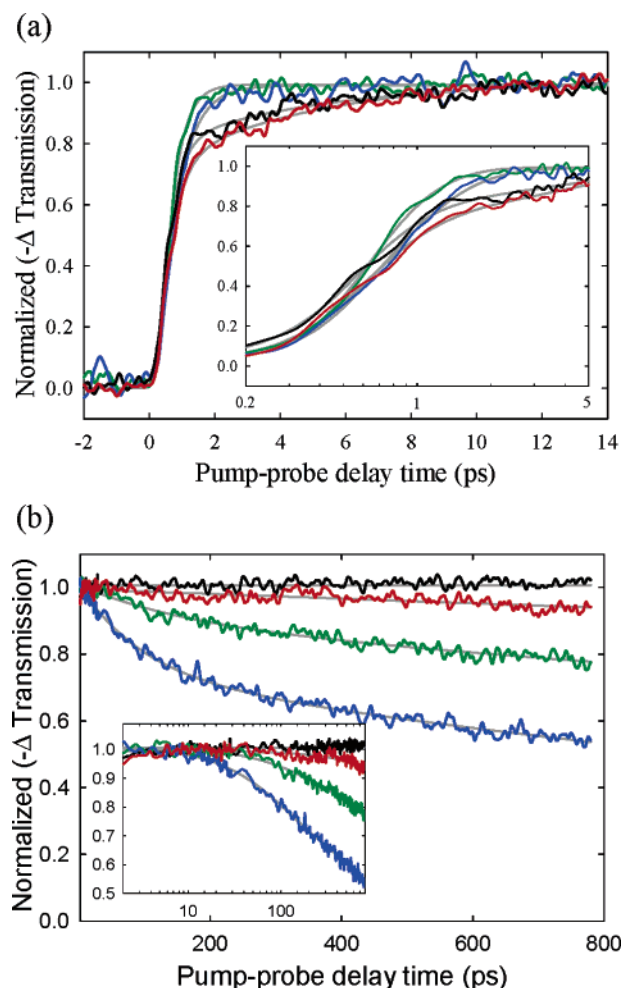


Figure 6. Normalized change in transmission ($\times -1$) as a function of pump-probe delay time, showing (a) electron photoinjection at short times and (b) decay over long times. Insets show the same data with time on a logarithmic scale. Traces for films with $\sim 1 \mu\text{m}$ grains (black), films with ~ 500 nm grains (red), nanowires (green), and nanoparticles (blue) are accompanied by fits shown in gray. Fit parameters are given in Table 2.

wurtzite with band edges at about the same wavelengths as the films,¹⁰ so we assume that the absorption coefficient and skin depth are similar to those of the films. No difference in absorption coefficient was seen after annealing.

To ensure accurate frequency-dependent conductivity measurements,¹⁶ the pump beam was expanded using a 5 cm focusing lens placed 18 cm from the sample, and a 2.5 mm diameter iris was centered at the sample. With the expanded pump beam, the maximum flux at the sample was 5×10^{14} photons $\text{pulse}^{-1} \text{ cm}^{-2}$. Electron generation is a single-photon process, as determined by the linear dependence of the electron density, N_e , on pump fluence, as shown in Figure 5b. The electron density was obtained from a fit of the unmodified Drude model to the frequency-dependent conductivity of the bulk, single-crystal ZnO. In addition, the amplitude of the terahertz difference waveform scales linearly with pump fluence. Our studies of ZnO wafer conductivity will be described in further detail elsewhere.

The creation of mobile electrons by absorption of photons, which we will designate electron photoinjection, occurs on sub-picosecond time scales. We have characterized both the onset and the decay of photoconductivity for four different morphologies: nanoparticles, nanowires, films with ~ 500 nm grains, and films with $\sim 1 \mu\text{m}$ grains. Figure 6a displays the normalized

TABLE 2: Parameters for Fits of Electron Injection and of Electron Density Decay^a

	$A_{1,\text{inj}}$	$\tau_{1,\text{inj}}$ (fs)	$A_{2,\text{inj}}$	$\tau_{2,\text{inj}}$ (ps)	$A_{1,\text{dec}}$	$\tau_{1,\text{dec}}$ (ps)	$A_{2,\text{dec}}$	$\tau_{2,\text{dec}}$ (ns)
nanoparticles	1	570	0		0.26	94	0.74	2.4
nanowires	1	390	0		0.11	160	0.89	5.6
film (500 nm grains)	0.71	370	0.29	4.6	0		1	13.6
film (1 μm grains)	0.79	370	0.21	4.9	0		1	>20

^a The first four columns (“inj” subscripts) are the weighting factors and characteristic times for the double-exponential rise to a maximum function, eq 7, used to fit the electron photoinjection data of Figure 6a. The last four columns (“dec” subscripts) are the weighting factors and characteristic times for the double-exponential decay, eq 8, used to fit the electron density decay data of Figure 6b.

injection within the first 14 ps of photoexcitation. The inset shows the same data with time on a logarithmic time scale. Nanowires and nanoparticles show purely ultrafast injection, with response almost as fast as the terahertz detector-limited response. Maximum photoconductivity is achieved within 3 ps of photoexcitation. Both films also have this ultrafast injection but with the addition of a second slower component. Films reach over 70% of their full conductivity after 1 ps but are still at only ~90% of the maximum after 5 ps. The normalized pump scans of the nanowires and nanoparticles are fit with a single-exponential rise to a maximum while the films are fit with the sum of two exponentials

$$\frac{(-\Delta T(t))}{\Delta T_{\text{max}}} = [A_{1,\text{inj}}(1 - e^{-t/\tau_{1,\text{inj}}}) + A_{2,\text{inj}}(1 - e^{-t/\tau_{2,\text{inj}}})] \otimes G_{\text{det}} \quad (7)$$

where the $A_{i,\text{inj}}$ ’s are weighting factors ($A_{1,\text{inj}} + A_{2,\text{inj}} = 1$) and the $\tau_{i,\text{inj}}$ ’s are time constants. The exponential terms are convoluted with a Gaussian function, G_{det} , with 500 fs width, which represents the detector response. The results of the fits are shown with gray lines in Figure 6a, and the parameters of the fits are given in Table 2. The ultrafast component for each of the samples has a time constant of ~400 fs. The slower component present in the films has a time constant of ~5 ps. No difference in photoinjection was detected between the annealed and as-grown samples for either the nanowires or the films. It is not clear whether the morphology or the microstructure is responsible for the additional slow component in the films.

The subsequent decay of the photoconductivity is directly related to the ZnO morphology. Figure 6b shows normalized pump scans over the first 800 ps after the photoexcitation pulse for the same four morphologies as in Figure 6a. The inset shows the decay on a logarithmic time scale. The continuous film with 1 μm grains shows photoconductivity that does not decay at all over the 800 ps measurement, while the film with 500 nm grains decays only slightly to about 95% of its maximum value after 800 ps. The mesoporous, smaller-grained nanowires and nanoparticles decay faster. The 200 nm diameter nanowires decay to 78% of their initial conductivity, and the 50 nm diameter nanoparticles decay to 55% of their initial conductivity after 800 ps. No difference in decay times was seen for annealed versus as-grown nanowires or films.

The pump scans indicate that trapping and recombination events that decrease the number of mobile electrons and reduce the photoconductivity take place primarily at surfaces and interfaces, while very little trapping and recombination occur in the “bulk” ZnO on the nanosecond time scale. Trapped electrons do not absorb terahertz radiation because the energy spacing between the trap state and the conduction band is too

large. At room temperature, kT is 6.5 THz, so electrons would be thermally excited out of shallow trap states more easily than they would be excited through absorption of terahertz radiation. The characteristic scattering time for photoinjected electrons for all of these ZnO morphologies is ~90 fs, as will be described below. This scattering time results in an electron mean free path of 21 nm, on the order of the grain size in nanoparticles and within 1 to 2 orders of magnitude of the grain sizes of the nanowires and polycrystalline films, respectively. Electrons can sample much of the volume of a nanoparticle, hop to neighboring nanoparticles, and interact with many surfaces/boundaries within the first tens to hundreds of picoseconds after photoexcitation. Evidently, only a small fraction of the interactions with surfaces results in trapping or recombination. Interactions with surfaces are less frequent with the larger-grained nanowires than those with nanoparticles, so the decay in photoconductivity is slower. Film grain size is quite large compared to the electron mean free path, so electron interactions with grain boundaries are rare, and the electron lifetime is significantly longer than that in the nanostructured ZnO.

The decays of photoconductivity in nanoparticles and nanowires are fit with the sum of two exponential terms, while the films are fit with a single exponential

$$\frac{(-\Delta T(t))}{\Delta T_{\text{max}}} = A_{1,\text{dec}} e^{-t/\tau_{1,\text{dec}}} + A_{2,\text{dec}} e^{-t/\tau_{2,\text{dec}}} \quad (8)$$

where the $A_{i,\text{dec}}$ ’s are weighting factors ($A_{1,\text{dec}} + A_{2,\text{dec}} = 1$) and the $\tau_{i,\text{dec}}$ ’s are decay time constants. Fits to the measured photoconductivity decay are shown in Figure 6b with fitted parameters listed in Table 2. Nanoparticles have an initial fast decay with a time constant 94 ps as well as a slower decay with a time constant 2.4 ns. Nanowires show similar behavior but on longer time scales, with a fast component of 160 ps and a slow component of 5.6 ns. Additionally, the nanowire fit is weighted more strongly toward the slow component than the nanoparticle fit, as demonstrated by the larger $A_{2,\text{dec}}$ of the nanowires. The films with 500 nm grains could be fit with a single-exponential decay with a 13.6 ns time constant, while the films with 1 μm grains decayed so slowly that the time constant could not be determined from an 800 ps measurement.

To further understand electron transport in ZnO nanostructures, the frequency-dependent complex photoconductivity was evaluated at several different pump–probe delay times. ZnO permittivity was extracted from measurements of the composite permittivity using the reverse Bruggeman EMA for both static and photoexcited samples. The photoexcited composite time-domain terahertz trace was calculated using the sum of the static composite trace and the photoexcitation difference scan. ZnO photoconductivity was calculated using the non-photoexcited and photoexcited ZnO permittivities for ϵ and η in eq 3, respectively. We emphasize that this *photoconductivity* is the increase in conductivity due to electron injection by photon absorption and is not the total conductivity of the sample. Photoconductivity was measured for ZnO nanoparticles and both annealed and as-grown nanowires and films at delay times of 5, 20, 100, and 400 ps. Figure 7 shows the real and imaginary components of the conductivity for each of the five samples at a pump–probe delay time of 20 ps. The annealed nanowires and annealed films have the highest and the second highest real photoconductivity, as shown in Figure 7a, while the as-grown nanowires, films, and nanoparticles are somewhat lower. All samples show positive real DC photoconductivity with photoconductivity increasing with increasing frequency. The imagi-

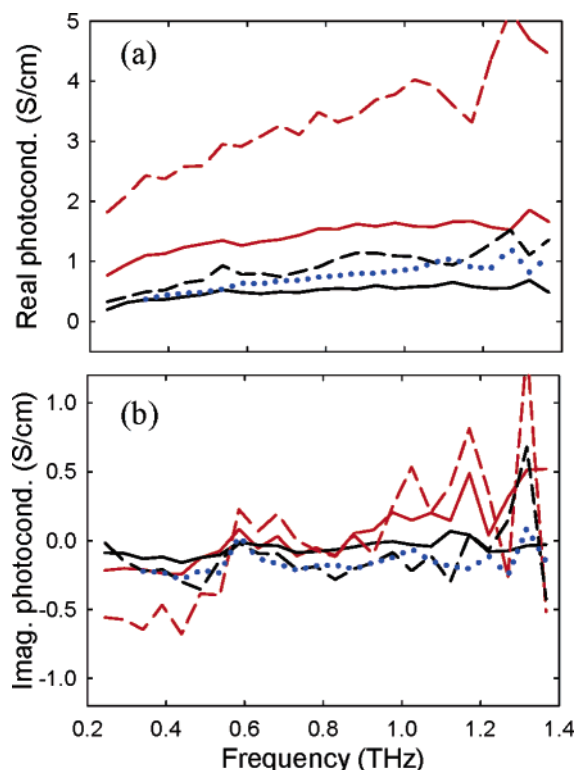


Figure 7. (a) Real and (b) imaginary components of the photoconductivity of ZnO samples at a pump-probe delay time of 20 ps. Solid lines are for ZnO films, dashed lines for nanowires, and blue dotted lines for nanoparticles. Black lines refer to as-grown samples, and red lines refer to annealed samples.

nary photoconductivity, Figure 7b, is negative for all samples at low frequency but becomes more positive with increasing frequency in each case, particularly for the annealed nanowires and films.

In addition to comparing the samples to each other at a given delay time, we also seek to understand the evolution of the conductivity as a function of time for a given sample. Figure 8 shows the complex photoconductivity for as-grown films, Figure 8a, and nanoparticles, Figure 8b, at each of the four delay times. The films show imaginary conductivities that are similar at all delay times, beginning at -0.1 S/cm at 0.25 THz and increasing with increasing frequency. Real conductivities are slightly positive at DC and increase with increasing frequency. The real conductivity at 5 ps is a bit lower than those for 20, 100, and 400 ps delay times. This difference is consistent with pump scans in Figure 6, which showed a slow component to the rise in photoconductivity such that it did not reach its maximum value until ~ 15 ps and which then maintained at least 95% of this maximum for more than 400 ps. Conversely, the nanoparticle pump scans showed a very fast rise in photoconductivity to a maximum value in less than 5 ps, followed by an exponential decay to about 60% of the maximum after 400 ps. This trend in conductivity is also reflected in the frequency-dependent photoconductivity data. Figure 8b shows that the 20 ps real photoconductivity is slightly larger than the 5 ps photoconductivity, with the 100 ps photoconductivity less than that at 5 ps and the 400 ps photoconductivity lower still. The imaginary photoconductivities are similar for all delay times, beginning at -0.2 S/cm at 0.35 THz and remaining fairly flat for all frequencies up to 1.4 THz.

As with the native conductivity, we use the Smith modification to the Drude model to account for this negative imaginary conductivity caused by preferential backscattering of electrons.

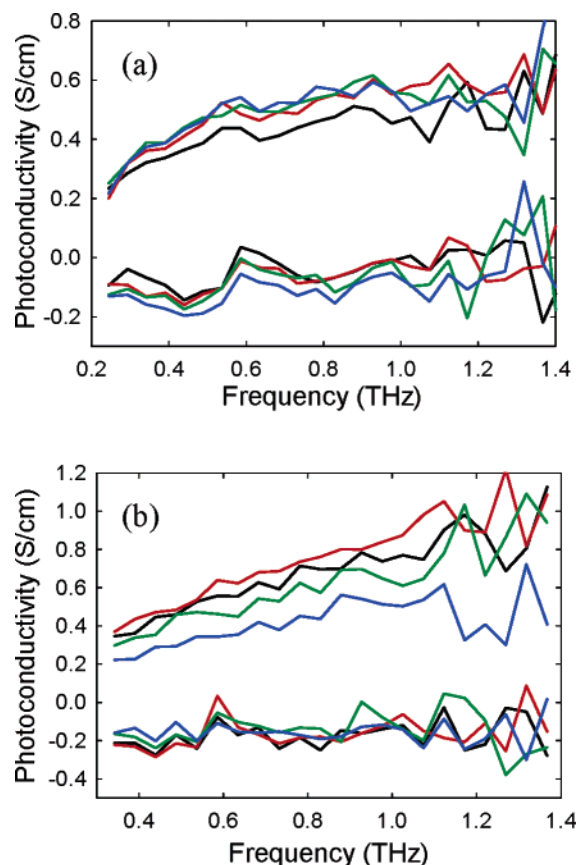


Figure 8. Photoconductivity of (a) as-grown films and (b) nanoparticles at pump-probe delay times of 5 ps (black), 20 ps (red), 100 ps (green), and 400 ps (blue). The upper group of lines is the real component of photoconductivity, and the lower group is the imaginary component for both parts a and b.

As mentioned previously, negative imaginary conductivity can also arise from the polarizability of excitons, although we do not believe excitons are the cause of the negative imaginary conductivity in our case. ZnO has a high exciton binding energy, ~ 60 meV, and so a significant portion of the optically excited electrons are expected to be bound as excitons. TRTS can detect excitons, and terahertz absorption attributed to excitonic polarization has been reported for ZnO wafers at temperatures below 150 K. Hendry et al. found that photoexcitation creates free electrons and holes that become bound as excitons through acoustic phonon emission over time scales ranging from a few picoseconds at 140 K to 40 ps at 30 K.²⁷ They report that the equilibrium ratio of free electrons to bound excitons increases with increasing temperature, with over 90% excitons at less than 100 K but over 90% free electrons at room temperature. Hendry models the excitonic photoconductivity by the Clausius-Mossotti relation, where both real and imaginary components go to zero at DC, with the real becoming more positive and the imaginary becoming more negative with increasing frequency.²⁷ It is unlikely that the negative imaginary conductivity shown here results from excitons, both because the shape of our conductivity curves does not show the excitonic signature found in the literature and because most electrons and holes would not be bound as excitons at room temperature.

The frequency-dependent, complex ZnO photoconductivity data are well fit with the Drude-Smith model for all morphologies, with or without annealing, and at all delay times. Figure 9 shows fits of this model to the annealed films (Figure 9a), as-grown nanowires (Figure 9b), and nanoparticles (Figure 9c), all at a delay time of 20 ps. As with the modeling of native

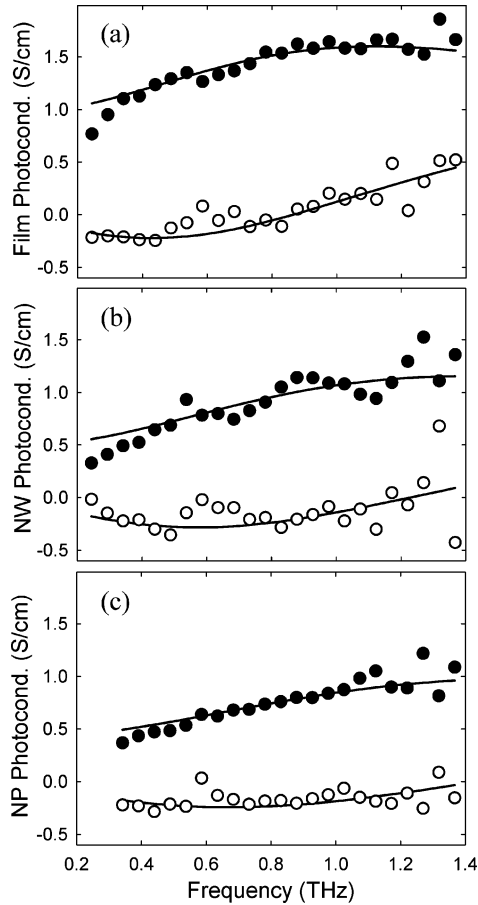


Figure 9. Drude–Smith fits (lines) to experimental photoconductivity (points) for (a) annealed ZnO film, (b) as-grown nanowires, and (c) nanoparticles at a pump–probe delay time of 20 ps. Solid circles are the real component of photoconductivity, and open circles are the imaginary component.

TABLE 3: Parameters for Drude–Smith Fit of Photoconductivity and Calculated DC Mobility^a

	N_e (10^{16} cm^{-3})	τ (fs)	c_1	μ ($\text{cm}^2 \text{ V}^{-1} \text{ s}^{-1}$)
annealed film	2.3	101	−0.68	232
film	1.1	93	−0.73	180
annealed NWs	6.6	88	−0.70	189
nanowires	2.0	84	−0.77	138
nanoparticles	2.0	77	−0.80	110

^a Electron density, scattering time, and persistence of velocity from the Drude–Smith model, eq 4, fit to measured photoconductivities of each ZnO sample. N_e values are for the 20 ps pump–probe delay time, and the τ and c_1 values are the averages of individual, unconstrained fits to data at 5, 20, 100, and 400 ps delay times. Data and example fits are shown in Figures 7 and 9, respectively. DC mobilities are calculated using τ and c_1 .

conductivity, the Drude–Smith model captures the magnitudes and shapes of the photoconductivity accurately using three fitting parameters: N_e , τ , and c_1 . The best-fit parameters for each of the five samples are given in Table 3. The parameters are similar for each of the five samples, with slight differences that correspond to expected trends in conductivity for different morphologies and annealing conditions.

All of the photoinjected electron densities are approximately $2 \times 10^{16} \text{ cm}^{-3}$, except for the annealed nanowires which are above $6 \times 10^{16} \text{ cm}^{-3}$. These densities are about a factor of 10 lower than the maximum amount expected from the photon flux and measured transmission. The discrepancy could be due to photons being scattered rather than absorbed or to generation

of immobile (trapped) electrons. The scattering times are all in the 80–100 fs range, while all c_1 parameters are between −0.68 and −0.80. Assuming 0.1 S/cm standard deviation for the conductivity data, typical 90% confidence intervals for these parameters are $\pm 30\%$ for N_e , ± 20 fs for τ , and ± 0.08 for c_1 . Although the confidence intervals nearly span the range of the data, the obvious trends in the fitted parameters indicate that the parameter determination is reliable, especially when used to compare the relative magnitudes of the parameters among samples. Some notable trends include the less negative c_1 for the annealed film and nanowires compared to their as-grown counterparts, indicating that annealing causes the ZnO to behave more Drude-like. For both the annealed and the as-grown sample sets, the films have less negative c_1 values than the nanowires, which in turn have less negative c_1 values than the nanoparticles, indicating more ideal Drude-like behavior for the larger-grained, less disordered samples. Similar trends are also apparent in the scattering times. The nanoparticles have the smallest scattering time, which may result from an increased frequency of reflections off of the particle surface compared to the larger-grained morphologies. Nanowires have somewhat larger scattering times, while the films have the largest scattering times. The trends in scattering times show the expected enhanced mobility in larger-grained, lower defect density, more ordered materials. The mean free paths calculated using room temperature thermal velocities from the scattering times are 23, 20, and 18 nm for the annealed film, nanowires, and nanoparticles, respectively. These mean free paths correspond roughly to Matthiessen’s rule⁴³

$$\frac{1}{l_{\text{eff}}} \geq \frac{1}{R_p} + \frac{1}{l_{\text{bulk}}} \quad (9)$$

which states that the effective mean free path, l_{eff} , will be reduced from the bulk mean free path, l_{bulk} , when particle radius, R_p , is on the order of l_{bulk} . The l_{eff} predicted from Matthiessen’s rule, calculated using $l_{\text{bulk}} = 23$ nm (the value determined for the 500 nm diameter grained films) are 20 nm for the 200 nm diameter nanowires and 13 nm for the 50 nm diameter nanoparticles. The larger measured l_{eff} compared to Matthiessen’s predicted l_{eff} for the nanoparticles is likely due to the wide distribution of particle sizes and a shift to larger effective particle size through sintering.

Comparing the parameters from the photoconductivity fits (Table 3) to those of the native conductivity fits (Table 1), we see that the native carrier concentration of the as-grown samples is 1–2 orders of magnitude larger than the carrier concentration created by photon absorption. The change in carrier concentration due to photon absorption is about the same as the carrier concentration of the annealed samples. The scattering times are larger and the c_1 values are less negative for the photoconductivity than for the native conductivity, indicating that electrons become more mobile as their concentration increases, at least in the relatively low concentration range studied here. The mobility of photoinjected electrons is $232 \text{ cm}^2 \text{ V}^{-1} \text{ s}^{-1}$ for the annealed films, about 3 times larger than the $80 \text{ cm}^2 \text{ V}^{-1} \text{ s}^{-1}$ for electrons present due to native defects. An increase in diffusion coefficient with increasing electron density has been observed in DSSCs, which is attributed to the filling of deep traps by a fraction of the electrons, allowing other electrons to move more freely.⁴⁴ Photoinjected electron mobilities range from $232 \text{ cm}^2 \text{ V}^{-1} \text{ s}^{-1}$ for annealed films to $110 \text{ cm}^2 \text{ V}^{-1} \text{ s}^{-1}$ for nanoparticle films, as listed in Table 3. Annealing the nanowires and films increases their mobilities by $\sim 50 \text{ cm}^2 \text{ V}^{-1} \text{ s}^{-1}$ compared to the respective as-grown samples. Mobilities in films are $\sim 40 \text{ cm}^2 \text{ V}^{-1} \text{ s}^{-1}$ greater than those in nanowires for both

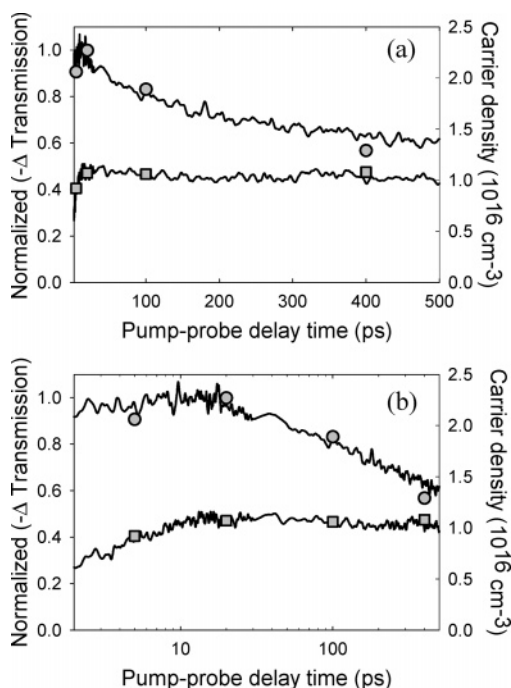


Figure 10. Normalized pump scans (lines) and carrier densities from Drude–Smith fits (points) with time on a (a) linear and (b) logarithmic scale. The upper line and circles are for nanoparticles; the lower line and squares are for as-grown films. The normalized film pump scan is multiplied by 0.48 to account for differences in N_e between the film and the nanoparticles.

the annealed and as-grown cases. The mobility in nanoparticle films is about half that of continuous films and about 60% that of annealed nanowires. The mobilities of the photoinjected electrons in the films and annealed nanowires are comparable to the value of $196 \text{ cm}^2 \text{ V}^{-1} \text{ s}^{-1}$ observed in ZnO nanowire field effect transistors where electron density is increased by supplying a gate bias voltage.⁴⁵ Electrons in ZnO nanoparticle films have similar scattering times but higher DC mobilities than those reported for TiO₂ nanoparticle films, owing to the smaller electron effective mass in ZnO than in TiO₂, 0.24 and 10, respectively. While both materials have scattering times of ~ 70 – 100 fs , ZnO mobility is at least 2 orders of magnitude larger than that of TiO₂, $110 \text{ cm}^2 \text{ V}^{-1} \text{ s}^{-1}$ compared to 0.01 – $1 \text{ cm}^2 \text{ V}^{-1} \text{ s}^{-1}$.^{3,4}

The complementary nature of the two types of pump–probe experiments is evident when we plot a pump scan along with the fitted electron densities calculated from the frequency-dependent photoconductivity. Figure 10 shows 800 ps pump scans on both linear and logarithmic time scales for the nanoparticles and the as-grown film along with the electron densities calculated by fitting the Drude–Smith model to the photoconductivity at each delay time. The individual points match the pump scans very closely. While τ and c_1 listed in Table 3 are the averages of the parameters given by unconstrained fits at each of the four delay times, each of the N_e plotted in Figure 10 result from fits done while holding τ and c_1 fixed at the tabulated average values. The agreement with the pump scans, which requires no model or workup, by the individual points further validates the methods and models that we have used to calculate photoconductivity as well as the accuracy of the fitted parameters.

Conclusions

We have shown that terahertz spectroscopy combined with effective medium theory can be used to determine the permit-

tivity of a nanostructured semiconductor embedded in a host matrix from measurements of the composite permittivity. By using this procedure, we can extract the semiconductor absorption coefficient, refractive index, and conductivity (either native or photoinduced). Specifically, we have shown that in our nanostructured ZnO materials annealing greatly reduces the electron concentration present as a result of native defects. Annealed thin films, nanowires, and nanoparticles all have absorption coefficients of nearly zero and refractive indices of 3, which match well with high-resistivity bulk ZnO values. Electron concentrations are $\sim 10^{18} \text{ cm}^{-3}$ in as-grown samples and $\sim 10^{16} \text{ cm}^{-3}$ in annealed samples. Photoexcitation causes an increase in electron density of $\sim 10^{16} \text{ cm}^{-3}$. The frequency-dependent photoconductivities of all ZnO morphologies are well fit with the Drude–Smith model. The model indicates that annealed samples and samples with larger grains tend to be more ideal conductors while smaller-grained or as-grown samples have higher scattering rates and more negative persistence of velocity, although on the whole the various samples are quite comparable. Conversely, pump scans indicate that morphology plays a very important role in electron lifetime. Photoconductivity stays nearly constant for almost 1 ns in continuous films, but for nanowires and nanoparticles it drops to 78% and 55% of its maximum value, respectively, after 800 ps.

The pump–probe studies presented here complement existing work on electron transport through the mesoporous semiconductor in DSSCs using IMPS or TOF methods by providing information on microscopic length scales and sub-nanosecond to sub-picosecond time scales. Preliminary DSSC studies suggest that nanowire arrays could offer improved transport compared to nanoparticle films,^{9,10,12} and our data support this conclusion. The frequency-dependent photoconductivity shows increased electron mobility in films and nanowires compared to nanoparticles at any given moment in time, and pump scans show that the inherent disorder and the multitude of interfaces in the nanoparticle films result in shorter electron lifetimes.

Acknowledgment. Acknowledgment is made to the donors of the American Chemical Society Petroleum Research Fund for partial support of this research through the Alternative Energy Postdoctoral Fellowship (PRF 43036-AEF) to J.B.B. C.A.S. acknowledges the National Science Foundation (Grant No. CHE-0135884) for partial support of this work.

References and Notes

- (1) Gratzel, M. *Nature* **2001**, *414*, 338.
- (2) Keis, K.; Magnusson, E.; Lindstrom, H.; Lindquist, S. E.; Hagfeldt, A. *Sol. Energy Mater. Sol. Cells* **2002**, *73*, 51.
- (3) Turner, G. M.; Beard, M. C.; Schmittenmaier, C. A. *J. Phys. Chem. B* **2002**, *106*, 11716.
- (4) Hendry, E.; Koeberg, M.; O'Regan, B.; Bonn, M. *Nano Lett.* **2006**, *6*, 755.
- (5) van de Lagemaat, J.; Frank, A. J. *J. Phys. Chem. B* **2001**, *105*, 11194.
- (6) Nelson, J. *Phys. Rev. B* **1999**, *59*, 15374.
- (7) Willis, R. L.; Olson, C.; O'Regan, B.; Lutz, T.; Nelson, J.; Durrant, J. R. *J. Phys. Chem. B* **2002**, *106*, 7605.
- (8) Tennakone, K.; Bandaranayake, P. K. M.; Jayaweera, P. V. V.; Konno, A.; Kumara, G. *Physica E* **2002**, *14*, 190.
- (9) Baxter, J. B.; Aydil, E. S. *Appl. Phys. Lett.* **2005**, *86*, 053114.
- (10) Baxter, J. B.; Walker, A. M.; van Ommering, K.; Aydil, E. S. *Nanotechnology* **2006**, *17*, S304.
- (11) Law, M.; Greene, L. E.; Johnson, J. C.; Saykally, R.; Yang, P. D. *Nat. Mater.* **2005**, *4*, 455.
- (12) Baxter, J. B.; Aydil, E. S. *Sol. Energy Mater. Sol. Cells* **2006**, *90*, 607.
- (13) Frank, A. J.; Kopidakis, N.; van de Lagemaat, J. *Coord. Chem. Rev.* **2004**, *248*, 1165.
- (14) Schlichthorl, G.; Park, N. G.; Frank, A. J. *J. Phys. Chem. B* **1999**, *103*, 782.

- (15) Benkstein, K. D.; Kopidakis, N.; van de Lagemaat, J.; Frank, A. J. *J. Phys. Chem. B* **2003**, *107*, 7759.
- (16) Beard, M. C.; Turner, G. M.; Schmittenmaer, C. A. *Phys. Rev. B* **2000**, *62*, 15764.
- (17) Vanexter, M.; Grischkowsky, D. *Appl. Phys. Lett.* **1990**, *56*, 1694.
- (18) Katzenellenbogen, N.; Grischkowsky, D. *Appl. Phys. Lett.* **1992**, *61*, 840.
- (19) Jepsen, P. U.; Schairer, W.; Libon, I. H.; Lemmer, U.; Hecker, N. E.; Birkholz, M.; Lips, K.; Schall, M. *Appl. Phys. Lett.* **2001**, *79*, 1291.
- (20) Beard, M. C.; Turner, G. M.; Schmittenmaer, C. A. *Nano Lett.* **2002**, *2*, 983.
- (21) Beard, M. C.; Turner, G. M.; Murphy, J. E.; Micic, O. I.; Hanna, M. C.; Nozik, A. J.; Schmittenmaer, C. A. *Nano Lett.* **2003**, *3*, 1695.
- (22) Choy, T. C. *Effective Medium Theory: Principles and Applications*; Clarendon Press: Oxford, U. K., 1999.
- (23) Black, M. R.; Lin, Y. M.; Cronin, S. B.; Rabin, O.; Dresselhaus, M. S. *Phys. Rev. B* **2002**, *65*, 195417.
- (24) Bruggeman, D. A. G. *Ann. Phys.* **1935**, *24*, 636.
- (25) Maxwell–Garnett, J. C. *Philos. Trans. R. Soc. London, Ser. A* **1904**, *203*, 385.
- (26) Azad, A. K.; Han, J. G.; Zhang, W. L. *Appl. Phys. Lett.* **2006**, *88*, 021103.
- (27) Hendry, E. Charge Dynamics in Novel Semiconductors. Ph.D. Thesis, University of Amsterdam, Amsterdam, 2005.
- (28) Webb, J. B.; Williams, D. F.; Buchanan, M. *Appl. Phys. Lett.* **1981**, *39*, 640.
- (29) Carcia, P. F.; McLean, R. S.; Reilly, M. H.; Nunes, G. *Appl. Phys. Lett.* **2003**, *82*, 1117.
- (30) Wan, Q.; Li, Q. H.; Chen, Y. J.; Wang, T. H.; He, X. L.; Li, J. P.; Lin, C. L. *Appl. Phys. Lett.* **2004**, *84*, 3654.
- (31) Huang, M. H.; Mao, S.; Feick, H.; Yan, H. Q.; Wu, Y. Y.; Kind, H.; Weber, E.; Russo, R.; Yang, P. D. *Science* **2001**, *292*, 1897.
- (32) Greene, L. E.; Law, M.; Goldberger, J.; Kim, F.; Johnson, J. C.; Zhang, Y. F.; Saykally, R. J.; Yang, P. D. *Angew. Chem., Int. Ed.* **2003**, *42*, 3031.
- (33) Greene, L. E.; Law, M.; Tan, D. H.; Montano, M.; Goldberger, J.; Somorjai, G.; Yang, P. D. *Nano Lett.* **2005**, *5*, 1231.
- (34) Brekhovskikh, L. M. *Waves in Layered Media*; Academic Press: London, 1960.
- (35) Kohan, A. F.; Ceder, G.; Morgan, D.; Van de Walle, C. G. *Phys. Rev. B* **2000**, *61*, 15019.
- (36) Hsu, J. W. P.; Tallant, D. R.; Simpson, R. L.; Missert, N. A.; Copeland, R. G. *Appl. Phys. Lett.* **2006**, *88*, 252103.
- (37) Look, D. C.; Reynolds, D. C.; Sizelove, J. R.; Jones, R. L.; Litton, C. W.; Cantwell, G.; Harsch, W. C. *Solid State Commun.* **1998**, *105*, 399.
- (38) Brus, L. E. *J. Chem. Phys.* **1984**, *80*, 4403.
- (39) Smith, N. V. *Phys. Rev. B* **2001**, *64*15, 155106.
- (40) Zhang, Z. Y.; Jin, C. H.; Liang, X. L.; Chen, Q.; Peng, L. M. *Appl. Phys. Lett.* **2006**, *88*, 073102.
- (41) Ellmer, K. J. *Phys. D: Appl. Phys.* **2001**, *34*, 3097.
- (42) Wolden, C. A.; Barnes, T. M.; Baxter, J. B.; Aydil, E. S. *J. Appl. Phys.* **2005**, *97*, 043522.
- (43) Mulvaney, P. *Langmuir* **1996**, *12*, 788.
- (44) Peter, L. M.; Wijayantha, K. G. U. *Electrochem. Commun.* **1999**, *1*, 576.
- (45) Ju, S. H.; Lee, K.; Janes, D. B. *Nano Lett.* **2005**, *5*, 2281.